3D Printing 18F Radioactive Phantoms for PET Imaging

Daniel Gillett (Daniel.gillett@Addenbrookes.nhs.uk)
Cambridge University Hospitals NHS Foundation Trust https://orcid.org/0000-0002-9773-6502

Daniel Marsden
Cambridge University Hospitals NHS Foundation Trust

Safia Ballout
Cambridge University Hospitals NHS Foundation Trust

Bala Attili
AstraZeneca R&D Cambridge

Nick Bird
Cambridge University Hospitals NHS Foundation Trust

Sarah Heard
Cambridge University Hospitals NHS Foundation Trust

Mark Gurnell
University of Cambridge

Iosif A Mendichovszky
Cambridge University Hospitals NHS Foundation Trust

Luigi Aloj
Cambridge University: University of Cambridge

Original research

Keywords: PET,3D printing,phantoms, qualitycontrol, F18

Posted Date: December 30th, 2020

DOI: https://doi.org/10.21203/rs.3.rs-136006/v1

3D printing ^{18}F radioactive phantoms for PET imaging

Daniel Gillett[1,2,*], Daniel Marsden[3], Safia Ballout[1], Bala Attili[4], Nick Bird[1], Sarah Heard[1], Mark Gurnell[2,5], Iosif A Mendichovszky[1,6] and Luigi Aloj[1,6]

[1] Department of Nuclear Medicine, Cambridge University Hospitals NHS Foundation Trust, Cambridge Biomedical Campus, Hills Road, Cambridge, CB2 0QQ, UK

[2] Cambridge Endocrine Molecular Imaging Group, University of Cambridge, Addenbrooke's Hospital, Hills Road, Cambridge, Biomedical Campus, Hills Road, Cambridge, CB2 0QQ, UK

[3] Clinical Engineering, Cambridge University Hospitals NHS Foundation Trust, Cambridge Biomedical Campus, Hills Road, Cambridge, CB2 0QQ, UK

[4] Clinical Pharmacology & Safety Sciences, AstraZeneca, Darwin Building, Cambridge Science Park Milton Road, Cambridge, CB4 0WG

[5] Metabolic Research Laboratories, Wellcome Trust-MRC Institute of Metabolic Science, Addenbrooke's Hospital, Hills Road, Cambridge, Biomedical Campus, Hills Road, Cambridge, CB2 0QQ, UK

[6] Department of Radiology, University of Cambridge, Cambridge Biomedical Campus, Hills Road, Cambridge, CB2 0QQ, UK.

* denoted corresponding author

Abstract (350 words)

Purpose:

Phantoms are routinely used in molecular imaging to assess scanner performance. However, traditional phantoms with fillable shapes do not replicate human anatomy. 3D printed phantoms have overcome this by creating phantoms which replicate human anatomy which can be filled with radioactive material. The problem with these is that small objects suffer from boundary effects and therefore boundary-free objects are desirable. The purpose of this study was to explore the feasibility of creating resin-based 3D printed phantoms using ^{18}F-FDG.

Methods:

Radioactive resin was created using an emulsion of printer resin and ^{18}F-FDG. A series of test objects were printed including twenty identical cylinders, ten spheres with increasing diameters (2 mm to 20 mm) and a double helix. Radioactive concentration uniformity, printing accuracy and the amount of leaching were assessed.

Results:

Creating radioactive resin was simple and effective. The radioactivity remained bound to the resin for the duration that it was radioactive. The radioactive concentration was uniform among identical objects; the CoV of the mean, max and total signal were 3.6%, 3.8% and 2.6%, respectively. The printed cylinders and spheres were found to be within 4% of the model dimensions. A double helix was successfully printed as a test for the printer and appeared as expected on the PET scanner. The amount of radioactivity leached into the water was measurable (0.72%) but not visible above background on the imaging.

Conclusions:

Creating an 18F-FDG radioactive resin emulsion is a simple and effective way to create boundary-free, accurate, complex 3D phantoms that can be imaged using a PET/CT scanner. This technique could be used to print clinically realistic phantoms, however, they are single use, and cannot be made hollow without an exit hole. Also, there is a small amount of leaching of the radioactivity to take into consideration.

Keywords

PET, 3D printing, phantoms, quality control, F18

Background

Molecular imaging is a key element of many diagnostic pathways, such as oncology - using ^{18}F-FDG (1), ^{68}Ga-PSMA (2), ^{99m}Tc-HDP (3) - and nuclear endocrinology - using ^{99m}Tc-sestamibi (4), ^{11}C-methionine (5–7) and ^{11}C-metomidate (8,9). The optimal functioning of single photon emission computed tomography (SPECT) and positron emission tomography (PET) scanners is ensured by regular quality control checks, many of which involve the use of objects called ‘phantoms’ (10). These phantoms need to be radioactive and are either made with long lived radionuclides (such as Cobalt-57 or Germanium-68) and supplied by commercial companies as sealed sources or have unsealed short-lived radionuclides added to water-fillable voids. Both types of phantoms usually comprise simple geometrical shapes containing one or more radioactive concentrations. The purpose of these phantoms is to check the performance of the scanners but they are not as useful when optimising clinical imaging protocols. This optimisation is either done directly on patient images or by imaging phantoms that approximate patient anatomy. Traditionally, phantoms are made up of fillable moulded shapes containing activity

distributions typically seen in clinical scans, but they do not usually replicate the complex shapes found in the human body. Recent developments in 3D printing has made it easier than ever to create more realistic phantoms (11).

3D printers have already been used to create fillable voids of replicate human anatomy (12,13). This technique has the advantage of being able to fashion the voids into any 3D-printable shape and it can be used to create patient-specific phantoms. The phantom voids are filled with radioactive materials in a liquid state (such as water) and this, in turn, requires the shape to have a solid boundary. However, this boundary affects the signal in the resulting images due to the partial volume effects and tracer displacement. Although the effect is insignificant when objects are large it becomes very important when the modelled object of interest is small due to the inherent spatial resolution of the imaging systems. Because of this, alternatives to fillable voids have been used to create boundary-free objects.

These boundary-free objects have been made using malleable materials or moulds and created using a range of materials such as wax (14) and gelatin (15). Despite having the advantage of having no boundary they are usually simple geometric shapes and, as with traditional phantoms, do not mimic human anatomy very well. However, two recent studies (16,17) utilised resin-based 3D printing to create radioactive phantoms that have no boundary and can take any 3D printable form. The authors labelled the resin with technetium-99m (^{99m}Tc) before printing and were able to show that the resulting object could be imaged using a gamma camera. In our work we explored the feasibility of creating resin-based 3D printed phantoms using the PET radionuclide fluorine-18 (^{18}F). In particular, we were interested in creating radioactive phantoms which would be difficult or impossible to create using a fillable void or mould.

Methods

Radioactive 3D printing technique

To create the radioactive resin, an emulsion between the resin and the 18F-FDG was obtained by vigorously mixing the two together. In preparation for this, approximately 200 MBq was drawn up and added to 100 ml of Prusa research UV cured resin. The amount of radioactivity required was estimated based on the duration of the steps involved prior to imaging to enable us to image with approximately 200 kBq/ml. The container was shaken vigorously for 10 seconds and the heated plate was set to 70℃ to remove air bubbles by gently heating the radioactive resin. For each print created for this study, the radioactive resin emulsion was then poured into the resin tank of the masked Stereolithography (SLA) 3D printer (SL1, Prusa Research, Prague, Czech Republic) and the print was started (Figure 1).

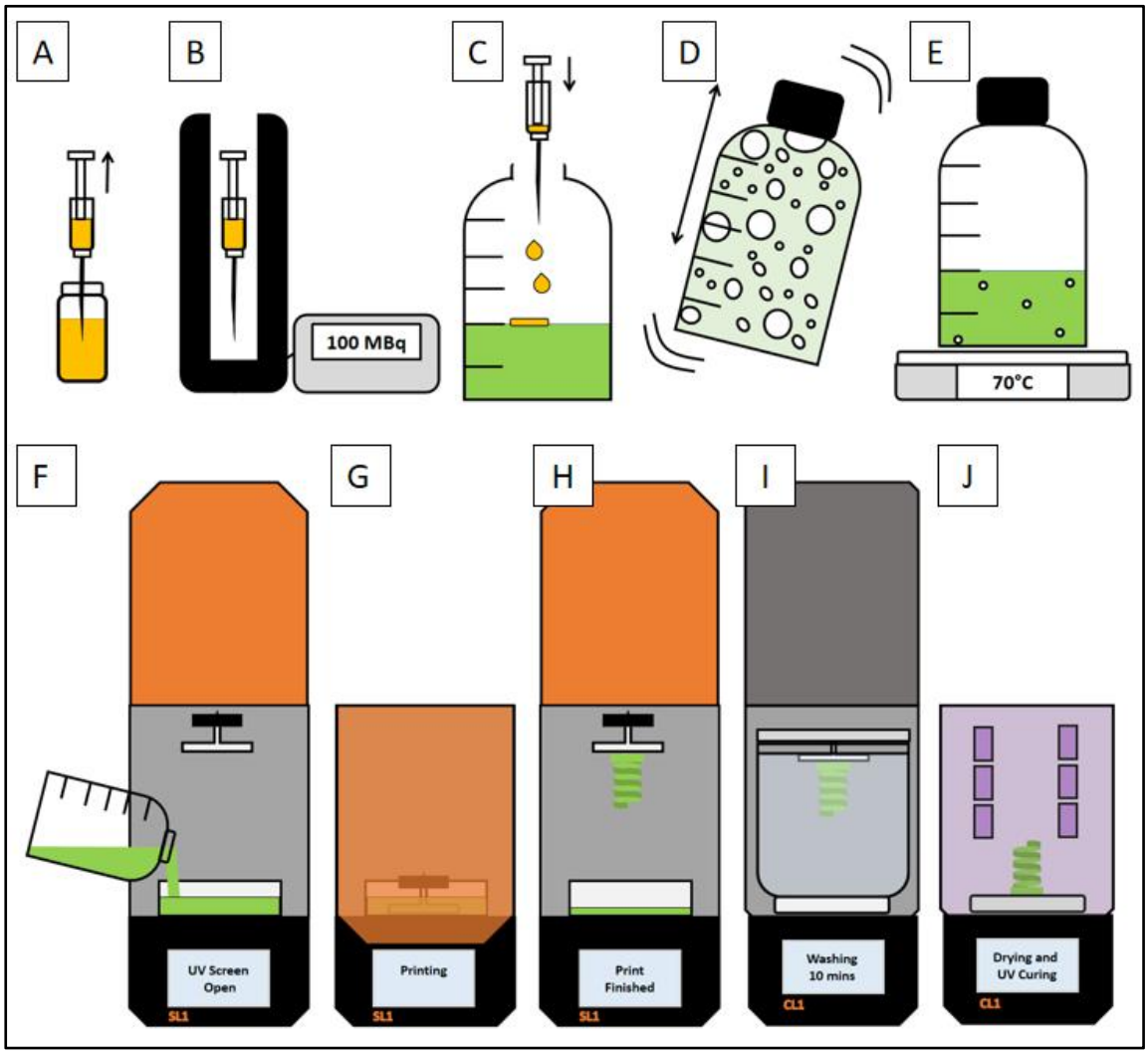

Figure 1 - 18F-FDG is drawn up into a syringe [A] and assayed using a radionuclide calibrator [B]. The required amount of 3D printing resin and the activity are added to a volumetric bottle [C]. The bottle is sealed and vigorously shaken for 10 seconds [D]. The bottle is placed on a heating plate for 10 minutes to prepare the resin for printing by helping to remove the bubbles [E]. The radioactive resin is added to the printer [F], the UV protective cover is closed [G] and the print is started. When the print is finished [H] the build plate is transferred to the lid of the IPA cleaning tank [I] and printed objects are cleaned for 10 minutes. After the washing the object is removed from the build plate and then dried using hot air and then cured with UV radiation for 5 minutes each [J].

At the end of the printing process the excess resin was removed by washing the object in isopropyl alcohol (IPA). Afterwards the object was removed from the build plate, air dried and then cured with UV light for 5 minutes (CL1 Curing and Washing Machine, Prusa Research, Prague, Czech Republic).

Radioactive concentration uniformity

Using Fusion 360 (Autodesk, California, United States) a cylinder with a 10 mm height and 8 mm diameter was created and exported as an STL file. The object was prepared for printing using PrusaSlicer (Prusa Research, Prague, Czech Republic) using print settings of an initial layer exposure time of 36 seconds, subsequent layer exposure times of 8 seconds and a layer height of 0.1 mm. This cylinder was printed twenty times using the radioactive resin (Figure 2A) to check the uniformity of the radioactive emulsion. The cylinders were imaged on a PET/CT scanner (Discovery 690 PET/CT scanner, GE Healthcare, Chicago, Illinois, United States). The images were reconstructed using ordered subsets expectation maximisation (OSEM) iterative reconstruction using 2 iterations and 24 subsets, time-of-flight (TOF), attenuation correction (AC) and a 2 mm gaussian filter. To analyse the uniformity from the cylinders twenty spherical volumes of interest (VOI), with a fixed diameter (2.9 cm), were centred at the maximum point within each cylinder. From these the mean, maximum and total signal were extracted and the coefficients of variation (CoV) calculated and used as a measure of the uniformity.

After imaging the cylinders were measured for 300 seconds in a sample counter (Wizard 2480 gamma counter, Wallac). The counts were background and decay corrected and then a mean, standard deviation, maximum and minimum counts were used to assess uniformity.

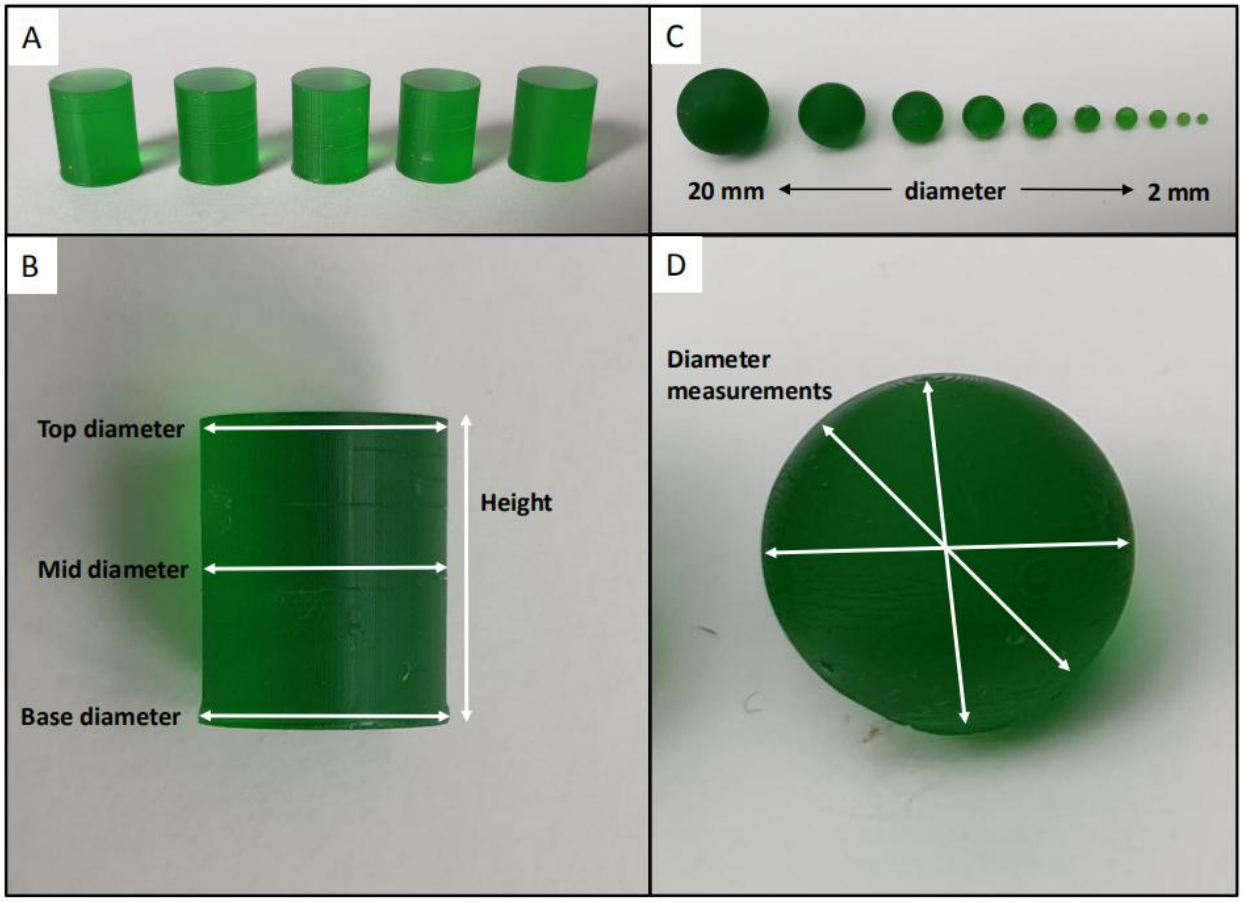

Figure 2 - Example of 5 out of the 20 printed cylinders [A] and the dimensions that were measured on each cylinder [B]. The printed spheres had nominal diameters of 20, 15, 12, 10, 8, 6, 5, 4, 3 and 2 mm [C] which were measured after printing at multiple orientations [D].

Test objects

Using Fusion 360 a set of test spheres with diameters of 2, 3, 4, 5, 6, 8, 10, 12, 15 and 20 mm (Figure 2C) were created and exported as STL files before preparing for printing using PrusaSlicer. These spheres were chosen to test the printing techniques ability to produce small, well defined objects that do not have inactive walls. The print settings were the same as for the cylinders. After printing they were imaged on the PET/CT scanner within a firm jelly to hold them in position and negate the need for support structures (Figure 4A-B). To make the jelly 60 grams

of powdered gelatin was added to 300 ml of cold water and heated to approximately 40℃ until it all dissolved. The heated solution was poured into a cylinder and left to set for 30 minutes in a freezer. Afterwards the spheres were set half into the surface of the jelly and then covered with more jelly, once again the jelly being left in the freezer to set.

A double helix (a 3D printing calibration object - https://www.thingiverse.com/thing:2980929) was prepared for printing using PrusaSlicer and printed using the same settings as for the cylinders. This calibration object was chosen because it is a complex shape that would be difficult to make as a void or from a mould and also is a difficult test of the printing capabilities of the 3D printing method using the modified resin. The double helix was mounted inside a cylinder which was then filled with water before acquiring a 10 min static acquisition in the PET/CT scanner. The images of the spheres and the helix were reconstructed using the same parameters as for the cylinders.

Printing Accuracy

We assessed printing accuracy by taking 10 measurements of the diameter of the printed spheres (Figure 2D) and the height and diameter of the cylinders (Figure 2B). These measurements were carried out using calibrated calipers to find the differences between the models and the printed spheres. From the measured diameters the volume of the spheres was calculated and compared to the volume of the models they were printed from.

Radioactivity leaching

We measured the amount of radioactivity that leached out of the double helix by taking a 2 ml sample 3 hours after the water was added to the cylinder. Using the volume of the cylinder and

the sensitivity of the gamma counter we were able to estimate the amount of leaching from the object.

Results

Creating radioactive resin was relatively simple using our emulsion technique. The emulsion was also very stable and we found that it remained mixed for much longer than it was radioactive. We were able to visualise this by assuming food colouring would bind in a similar way to the FDG. After creating an emulsion with both FDG and food colouring we observed the degree of separation. After one month our sample was still mixed.

The cylinders used for the uniformity assessment were printed in 24 minutes and imaged using the PET/CT scanner. From the PET/CT images of the cylinders, the CoV of the mean, max and total signal were calculated to be 3.6%, 3.8% and 2.6% respectively. The CoV of the counts measured from the cylinders by the sample counter was found to be 0.70% and comparable to the expected CoV based on the mean number of counts of the samples of 0.12% (assuming the expected standard deviation of the counts is approximately the square root of the counts). Figure 3 shows the radioactive uniformity as shown by each sample's deviation from the corrected mean counts. From these measurements we found that the maximum deviation from the mean was 1.65%.

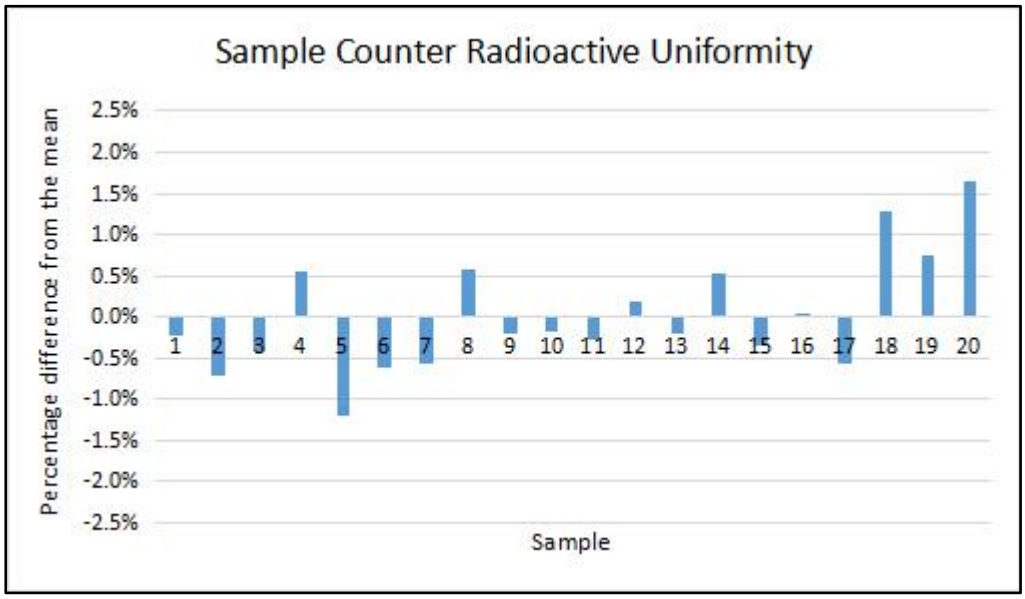

Figure 3 - Chart showing the percentage differences from the mean counts acquired by the sample counter.

To assess printing accuracy the cylinders had measurements taken of the height, base diameter, mid diameter and top diameter (Figure 2B) which were compared to the model dimensions (Height - 10 mm and diameter - 8 mm). The mean, standard deviation and percentage difference of the measurements were 9.92 mm (sd 0.02, %dif -0.82), 8.27 mm (sd 0.05 mm, Δ 3.38%), 8.01 (sd 0.01 mm, Δ 0.011%) and 8.03 mm (sd 0.01, Δ 0.35%) mm for the height, base, mid and top diameters respectively The data is summarised in table 1.

Printing Accuracy	**Height**	**Base diameter**	**Mid diameter**	**Top diameter**
Model (mm)	*10.00*	*8.00*	*8.00*	*8.00*
Mean (mm)	9.92	8.27	8.01	8.03

SD (mm)	0.02	0.05	0.01	0.01
Difference (%)	-0.8%	3.4%	0.1%	0.4%

Table 1 - Differences of the measured dimensions from the model they were printed from.

The spheres were printed in 43 minutes, were imaged using the PET/CT scanner and used to assess printing accuracy. Ten measurements of the diameters were taken and compared to the computer models. The mean differences and percentage differences were -0.074 mm (-3.7%), -0.113 mm (-3.8%), -0.129 mm (-3.2%), -0.063 mm (-1.3%), -0.037 mm (-0.6%^), -0.097 mm (-1.2%), -0.033 mm (-0.3%), -0.083 mm (-0.7%), -0.095 mm (-0.6%) and -0.178 mm (-0.9%) for the 2, 3, 4, 5, 6, 8, 10, 12, 15 and 20 mm diameter spheres respectively. The data is summarised in table 2.

Sphere diameter (mm)	**2**	**3**	**4**	**5**	**6**	**8**	**10**	**12**	**15**	**20**
Diameter Measurement mean (mm)	1.93	2.89	3.87	4.94	5.96	7.90	9.97	11.92	14.91	19.82
Absolute difference (mm)	-0.074	-0.113	-0.129	-0.063	-0.037	-0.097	-0.033	-0.083	-0.095	-0.178
Percentage difference (%)	-3.7	-3.8	-3.2	-1.3	-0.6	-1.2	-0.3	-0.7	-0.6	-0.9

Table 2 - Sphere diameter measurements.

All of the spheres were visible on CT (Figure 4C) and PET (Figures 4B & 4D). In the reconstructed dataset each sphere was outlined using the thresholding tool to create a VOI. The max signal within each VOI was used as a measure of recovery. Figure 5 shows a bar chart of the max signal vs the sphere diameter. As expected, due to the reconstruction algorithm, scanner limitations and the partial volume effect, there is a convergence towards the actual concentration as the spheres get larger.

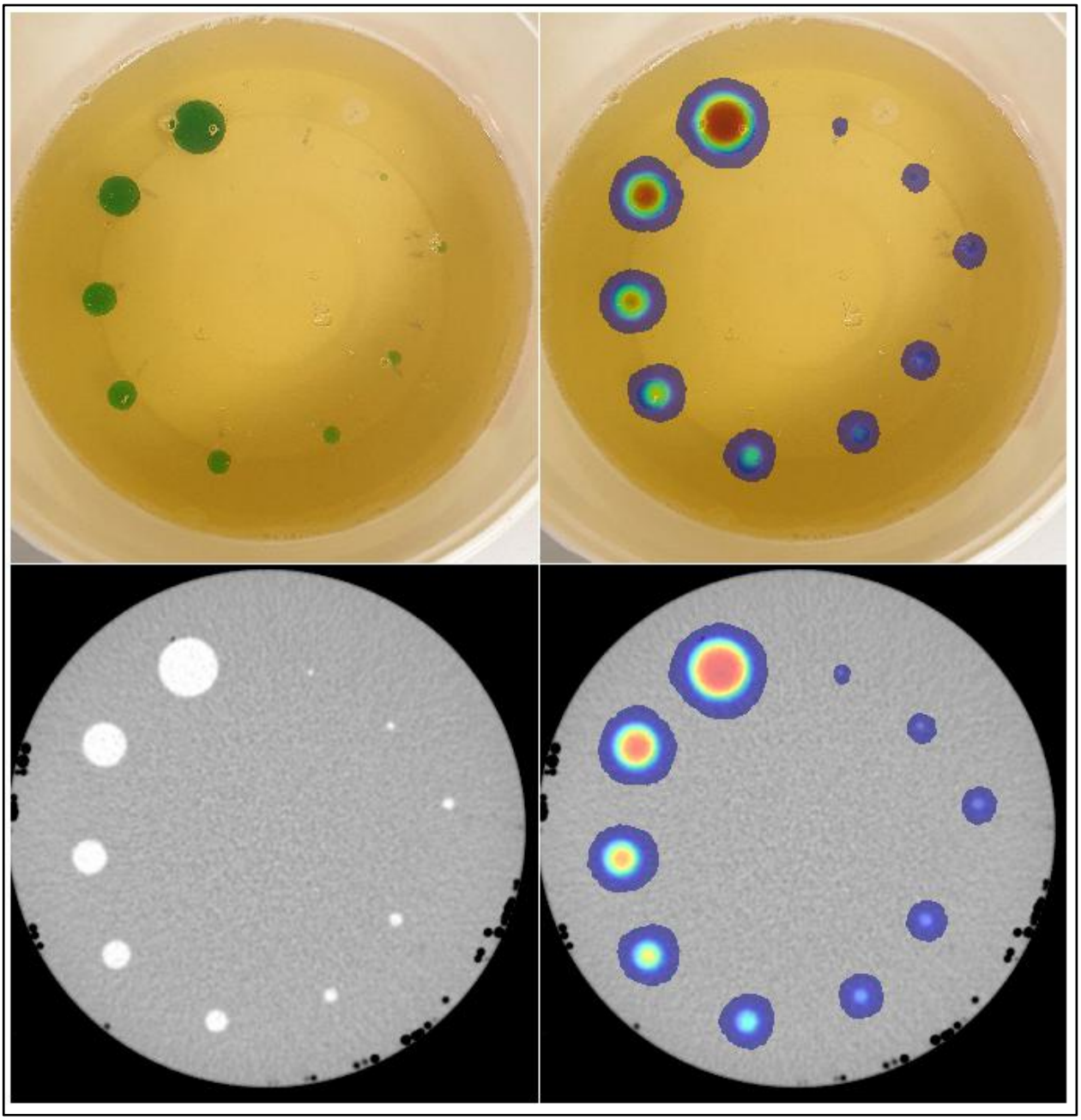

Figure 4 - A - Spheres in gelatin mixture, B - Spheres in gelatin mixture with PET signal overlaid, C - CT of spheres and D - PET/CT images of spheres.

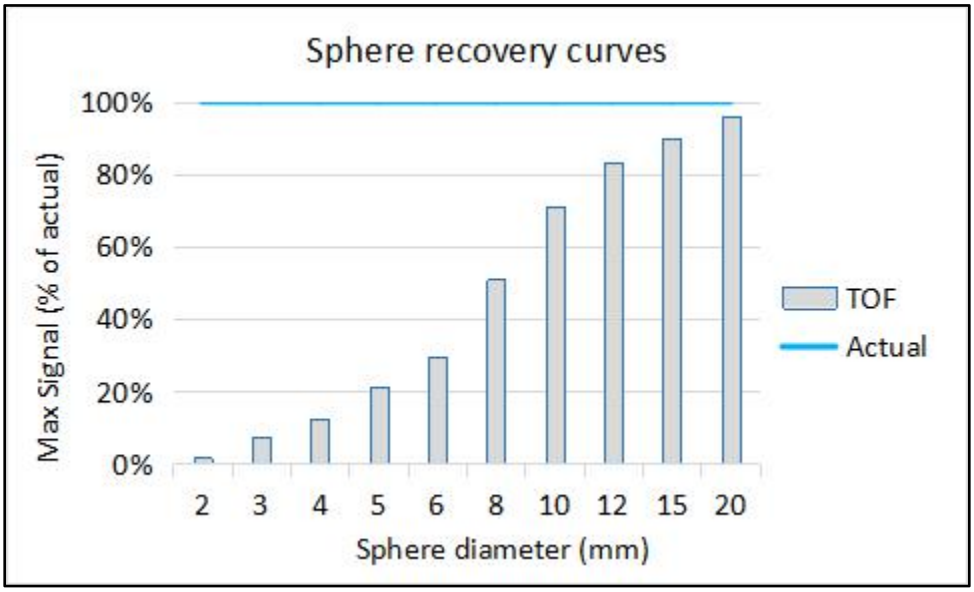

Figure 5 - Bar chart showing the max signal from each sphere compared with the actual concentration.

The helix was printed in 194 minutes and then successfully imaged using the PET/CT scanner and appeared as expected. The base and the coils were easily visible and the horizontal bars were not seen distinctly. Most importantly the appearance of the radioactive concentration was consistent throughout the height of the double helix.

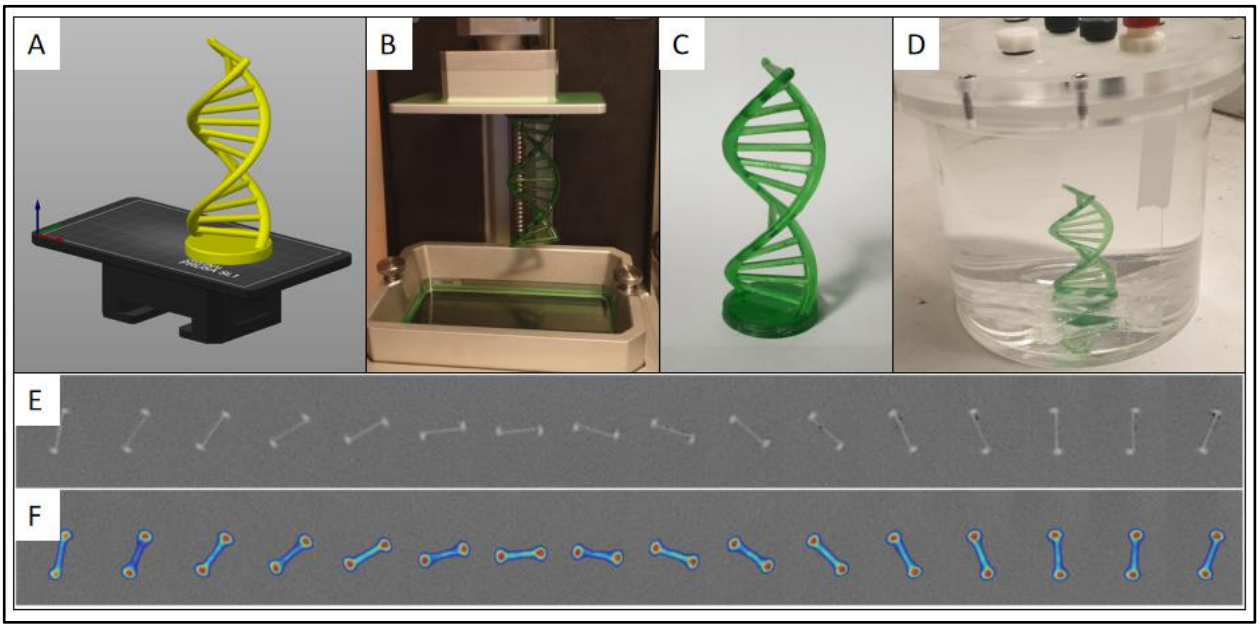

Figure 6 - A - Helix model prepared for printing in PrusaSlicer. B - Helix after printing. C - Helix after removal from build plate, washed, dried and cured. D - Helix mounted in a cylinder of water for imaging. E - Axial CT slices. F - Axial PET/CT slices.

The amount of radioactivity that leached into the water of the phantom was 0.72% of the activity in the helix. This was calculated by taking a sample from the water at 3 hours after the phantom (Figure 5D) being in the water. This activity was not visible above the background count rate on the scanner.

Discussion

We have, for the first time, demonstrated that radioactive PET phantoms can be created using a consumer SLA 3D printer and that it can be used to create phantoms that are complex in their shape and structure. This may allow to better mimic human anatomy and simulate heterogeneous radioactivity concentrations that are normally present in the *in vivo* setting.

The printing process seemed unaffected by the presence of the radioactivity and the carrier liquid, however we still found limitations to the technique, most notably the ability to print large solid blocks (Figure 7). We tried to do this to test the uniformity using the scanner and so printed a cuboid that was slightly smaller than the build plate. However this did not produce the expected shape because the resin tends to shrink by a few microns after being cured and when the volume is large this causes the edges of some layers not to adhere to each other, resulting in cracks. This is a known limitation of SLA 3D printing which may have been made worse by the addition of radioactive carrier liquid. This means that this particular method is unsuitable for creating large solid objects. It does appear suitable, however, for generating small to medium sized intricate shapes that would be difficult or even impossible to make with conventional techniques such as fillable voids or moulds.

We were able to create phantoms using ^{18}F despite its short half life because the 3D printer used masked SLA technology. This technology uses an LCD to mask a UV light to the shape required for each layer. This means that compared to conventional SLA printing - which uses a laser point to trace each layer - it is quicker. The limiting factor is therefore the height of the object being printed but using this technology we were able to print the helix object (Figure 6) which was 95 mm high in 194 minutes (i.e. 0.48mm/min). At this rate an object the maximum size of the printer could be printed in 5 hours but more importantly smaller objects such as the uniformity cylinders (Figure 2A) and spheres, up to 20 mm in diameter, (Figure 2C) can be printed in just 24 and 43 minutes respectively, no matter how many there are.

The uniformity of the radioactivity within the test objects (Figure 2A) was very good and more than adequate for the purposes of making phantoms that replicate typical radioactivity concentrations in patients. This result has given us confidence in the technique to use it for image optimisation instead of or in combination with water filled phantoms.

We were able to print accurate spheres as small as 2 mm in diameter with a well defined activity concentration and without an inactive boundary (Figure 2C and 4). This ability will enable phantoms to be made that mimic the anatomy and pathology that we see clinically in investigations such as pituitary (5-7) and adrenal (8, 9) adenoma localisation that has not been possible before. Phantoms like these are critical in optimising imaging protocols because traditional phantoms that use fillable voids have relatively thick inactive walls and therefore cannot get close to approximating the shapes and proximity of the small anatomical structures being imaged in these investigations.

The printing accuracy was remarkably precise with the maximum deviation of the model being 0.27 mm (3.4%) at the bottom of the cylinder (Figure 5). This is an effect caused by the longer exposure time for the first layer. The longer exposure is required to ensure the print is fixed securely to the build plate but also results in more resin being cured by scattered UV light. The effect is not seen as the cylinder is printed with the mid and top diameters being within 0.01 ± 0.01 mm and 0.03 ± 0.01mm respectively. Although small this deviation could be accounted for by adjusting the model. The small amount of shrinkage observed in the heights of the cylinders could also be adjusted for by enlarging the height of the model however given that the deviation in the height and the bottom diameter are both far smaller than the resolution of the scanner it is not felt that this will have a noticeable or measurable effect on the final image.

The helix demonstrated that complex objects can be printed and imaged using a PET scanner (Figure 6). There are no structures within the human body that could be approximated with a helix but nevertheless it acted as a potential worst case scenario for the printer because it had multiple overhanging bridges and was relatively tall (95 mm). As many biological structures are smaller than this it showed that there is real clinical potential to be gained by being able to

optimise a PET scan using the radionuclide most commonly used, in the shape and concentration found in clinical practice.

The amount of leaching of the radioactivity into the background was relatively low (<1%) although was measurable in the background of the phantom. The size of the phantom was large relative to the printed object and so did not represent a problem however more work is needed to determine whether the amount of leaching would be a problem for smaller background volumes. Although there is no requirement for these phantoms to be in a water-filled background this is a potential limitation (Figure 7) if this is how they are to be utilised.

It is theoretically possible to create phantoms of any printable shape and size and as already mentioned this included a vast range of options but there are limitations with what is printable using this technique (Figure 7). In addition to the limitations already mentioned it is not possible to print shapes that are hollow and completely sealed. Without a hole in the hollow structure excess resin will be captured and have no way of being removed therefore an exit hole must always be included in this type of structure.

Advantages
- No inactive walls
- Accurate geometry
- Can print complex 3D shapes
- Short print times

Limitations
- Cannot print large solid objects
- Phantoms are single use
- Small amount of radioactivity leaching into water
- Cannot print hollow objects without an exit hole

Figure 7 - Advantages and limitations of radioactive 3D printing technique.

Conclusion

We have demonstrated that creating a radioactive resin emulsion is a simple and effective way to create boundary-free 3D phantoms that can be imaged using a PET/CT scanner. Our method is quick enough to use widely available 18F-FDG and could be used to create any SLA 3D printable object.

Abbreviations

^{11}C - carbon-11

^{18}F - fluorine-18

^{99m}Tc - technetium-99m

kBq - kilobequercels

MBq - megabecquerel

SLA - Stereolithography

STL - Standard Tessellation Language

CT - Xray Computed Tomography

FDG - Fluorodeoxyglucose

IPA - isopropyl alcohol

PET - Positron Emission Tomography

SPECT - single photon emission tomography

UV - Ultraviolet radiation

OSEM - ordered subsets expectation maximisation

AC - attenuation correction

TOF - time-of-flight

CoV - coefficient of variation

VOI - volume of interest

Declarations

Ethics approval and consent to participate

Not applicable

Consent for publication

Not applicable

Availability of data and material

The datasets used and/or analysed during the current study are available from the corresponding author on reasonable request.

Competing interests

Not applicable

Funding

Funding for this work was awarded by Addenbrooke's Charitable Trust (ACT), the Alborada Trust and Dr Murthy Renduchintala. It makes up part of the Methods Of creating Radioactive Phantoms for accurate Human Simulation using 3D printing (MORPH-3D) project.

Authors' contributions

DG and DM developed the initial project design. DG, DM and LA were co-applicants on grant application. DG, BA and LA contributed to the method used for making the resin radioactive. DG and SB performed radioactive 3D printing. DG, SB and NB imaged the 3D printed phantoms. DG, NB, SH, IM and LA contributed to the study design and data analysis. DG, DM, SB, BA, NB, SH, IM, MG and LA all contributed to the writing of the manuscript. DG and MG contributed to the figures.

Acknowledgements

The authors would like to acknowledge the ACT team, for their help with securing the grant and handling the funds afterwards, and Bethany Gillett for her help, advice and support with the study design and writing of the manuscript.

References

1. Chen H, Pang Y, Wu J, Zhao L, Hao B, Wu J, et al. Comparison of [68Ga]Ga-DOTA-FAPI-04 and [18F] FDG PET/CT for the diagnosis of primary and metastatic lesions in patients with various types of cancer. Eur J Nucl Med Mol Imaging. 2020 Jul;47(8):1820–

372 32.Läppchen T, Meier LP, Fürstner M, et al. 3D printing of radioactive phantoms for nuclear
373 medicine imaging. *EJNMMI Phys*. 2020;7(1):22. Published 2020 Apr 22.
374 doi:10.1186/s40658-020-00292-0
375 2. Wester H-J, Schottelius M. PSMA-Targeted Radiopharmaceuticals for Imaging and Therapy.
376 Semin Nucl Med. 2019;49(4):302–12.
377 3. Nakajima K, Edenbrandt L, Mizokami A. Bone scan index: A new biomarker of bone
378 metastasis in patients with prostate cancer. Int J Urol Off J Jpn Urol Assoc. 2017;24(9):668–
379 73.
380 4. Redman S, Graham R, Little D. Parathyroid scintigraphy. Nucl Med Commun. 2019
381 Sep;40(9):e1–3.
382 5. Koulouri O, Kandasamy N, Hoole AC, Gillett D, Heard S, Powlson AS, et al. Successful
383 treatment of residual pituitary adenoma in persistent acromegaly following localisation by
384 11C-methionine PET co-registered with MRI. Eur J Endocrinol [Internet]. 2016;175(5).
385 Available from: https://eje.bioscientifica.com/view/journals/eje/175/5/485.xml
386 6. Koulouri O, Hoole AC, English P, Allinson K, Antoun N, Cheow H, et al. Localisation of an
387 occult thyrotropinoma with 11C-methionine PET-CT before and after somatostatin analogue
388 therapy. Lancet Diabetes Endocrinol. 2016;4(12):1050.
389 7. Bashari WA, Senanayake R, Fernández-Pombo A, Gillett D, Koulouri O, Powlson AS, et al.
390 Modern imaging of pituitary adenomas. Best Pract Res Clin Endocrinol Metab.
391 2019;33(2):101278.
392 8. Hennings J, Sundin A, Hägg A, Hellman P. 11 C-metomidate positron emission tomography
393 after dexamethasone suppression for detection of small adrenocortical adenomas in primary
394 aldosteronism. Langenbecks Arch Surg. 2010;395(7):963–7.
395 9. O'Shea PM, O'Donoghue D, Bashari W, Senanayake R, Joyce MB, Powlson AS, et al.
396 11C‐Metomidate PET/CT is a useful adjunct for lateralization of primary aldosteronism in

397 routine clinical practice. Clin Endocrinol (Oxf). 2019;90(5):670–9.
398 10. Madsen MT, Sunderland JJ. Nuclear Medicine and PET Phantoms. In: DeWerd LA, Kissick
399 M, editors. The Phantoms of Medical and Health Physics: Devices for Research and
400 Development [Internet]. New York, NY: Springer; 2014 [cited 2020 Aug 8]. p. 201–22.
401 (Biological and Medical Physics, Biomedical Engineering). Available from:
402 https://doi.org/10.1007/978-1-4614-8304-5_11
403 11. Filippou V, Tsoumpas C. Recent advances on the development of phantoms using 3D
404 printing for imaging with CT, MRI, PET, SPECT, and ultrasound. Med Phys.
405 2018;45(9):e740–60.
406 12. Gear JI, Long C, Rushforth D, Chittenden SJ, Cummings C, Flux GD. Development of
407 patient-specific molecular imaging phantoms using a 3D printer. Med Phys.
408 2014;41(8Part1):082502.
409 13. Robinson AP, Tipping J, Cullen DM, Hamilton D, Brown R, Flynn A, et al. Organ-specific
410 SPECT activity calibration using 3D printed phantoms for molecular radiotherapy dosimetry.
411 EJNMMI Phys. 2016 Dec;3(1):12.
412 14. Bazañez-Borgert M, Bundschuh RA, Herz M, Martínez M-J, Schwaiger M, Ziegler SI.
413 Radioactive spheres without inactive wall for lesion simulation in PET. Z Med Phys.
414 2008;18(1):37–42.
415 15. Kao YH, Luddington OS, Culleton SR, Francis RJ, Boucek JA. A Gelatin Liver Phantom of
416 Suspended 90Y Resin Microspheres to Simulate the Physiologic Microsphere
417 Biodistribution of a Postradioembolization Liver. J Nucl Med Technol. 2014 Dec
418 1;42(4):265–8.
419 16. Läppchen T, Meier LP, Fürstner M, Prenosil GA, Krause T, Rominger A, et al. 3D printing of
420 radioactive phantoms for nuclear medicine imaging. EJNMMI Phys [Internet]. 2020 Apr 22
421 [cited 2020 Nov 22];7. Available from:
422 https://www.ncbi.nlm.nih.gov/pmc/articles/PMC7176799/

17. Gear JI, Cummings C, Sullivan J, Cooper-Rayner N, Downs P, Murray I, et al. Radioactive 3D printing for the production of molecular imaging phantoms. Phys Med Biol. 2020 Sep 8;65(17):175019.

Figures

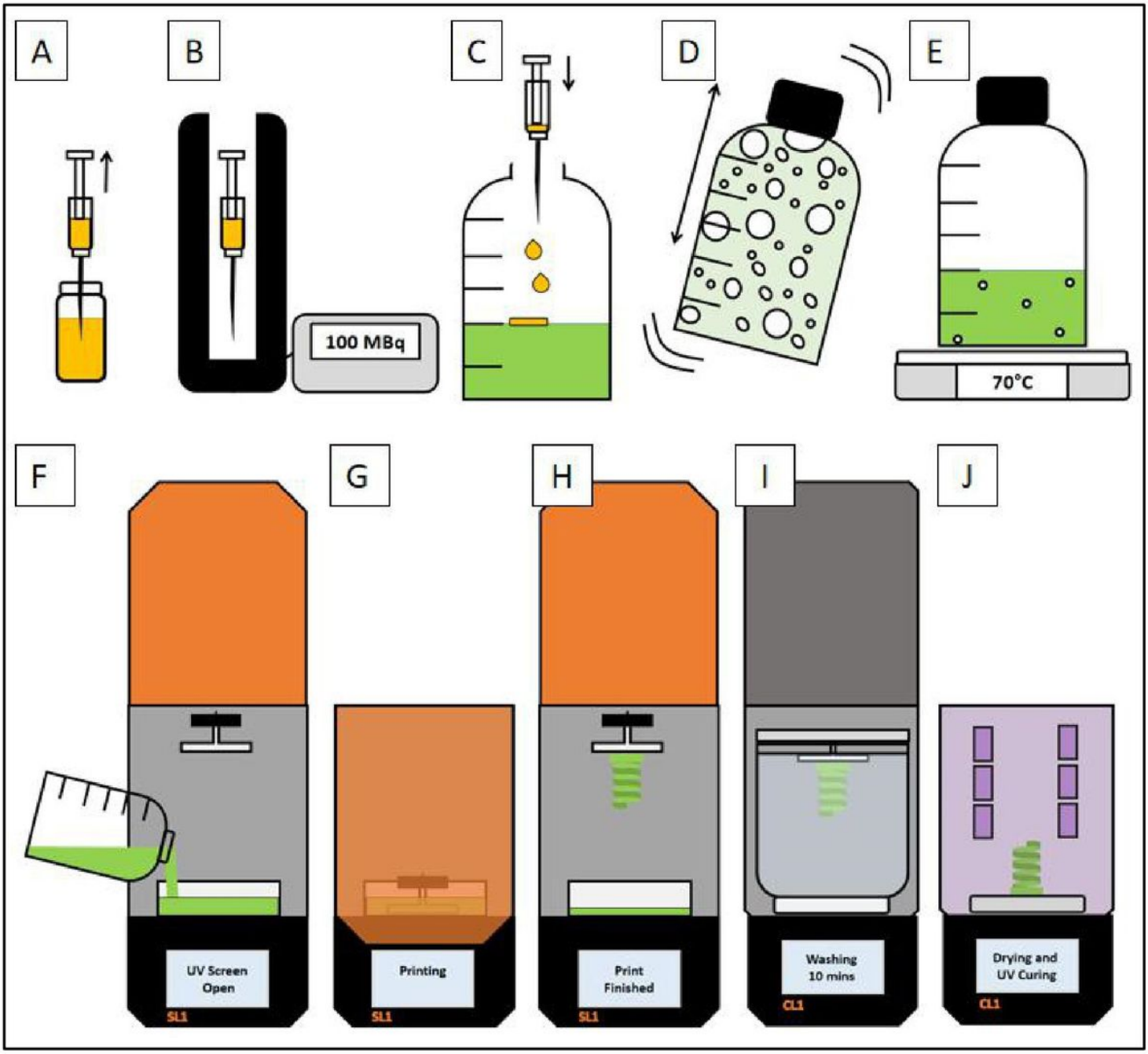

Figure 1

18F-FDG is drawn up into a syringe [A] and assayed using a radionuclide calibrator [B]. The required amount of 3D printing resin and the activity are added to a volumetric bottle [C]. The bottle is sealed and vigorously shaken for 10 seconds [D]. The bottle is placed on a heating plate for 10 minutes to prepare the resin for printing by helping to remove the bubbles [E]. The radioactive resinis added to the printer [F], theUV protective cover is closed [G] and the print is started. When the print is finished [H] the build plate is transferred to the lid of the IPA cleaning tank[I] and printed objectsare cleaned for 10 minutes. After the

washing the object is removed from the build plate and then dried using hot air and then curedwith UV radiation for 5 minutes each [J].

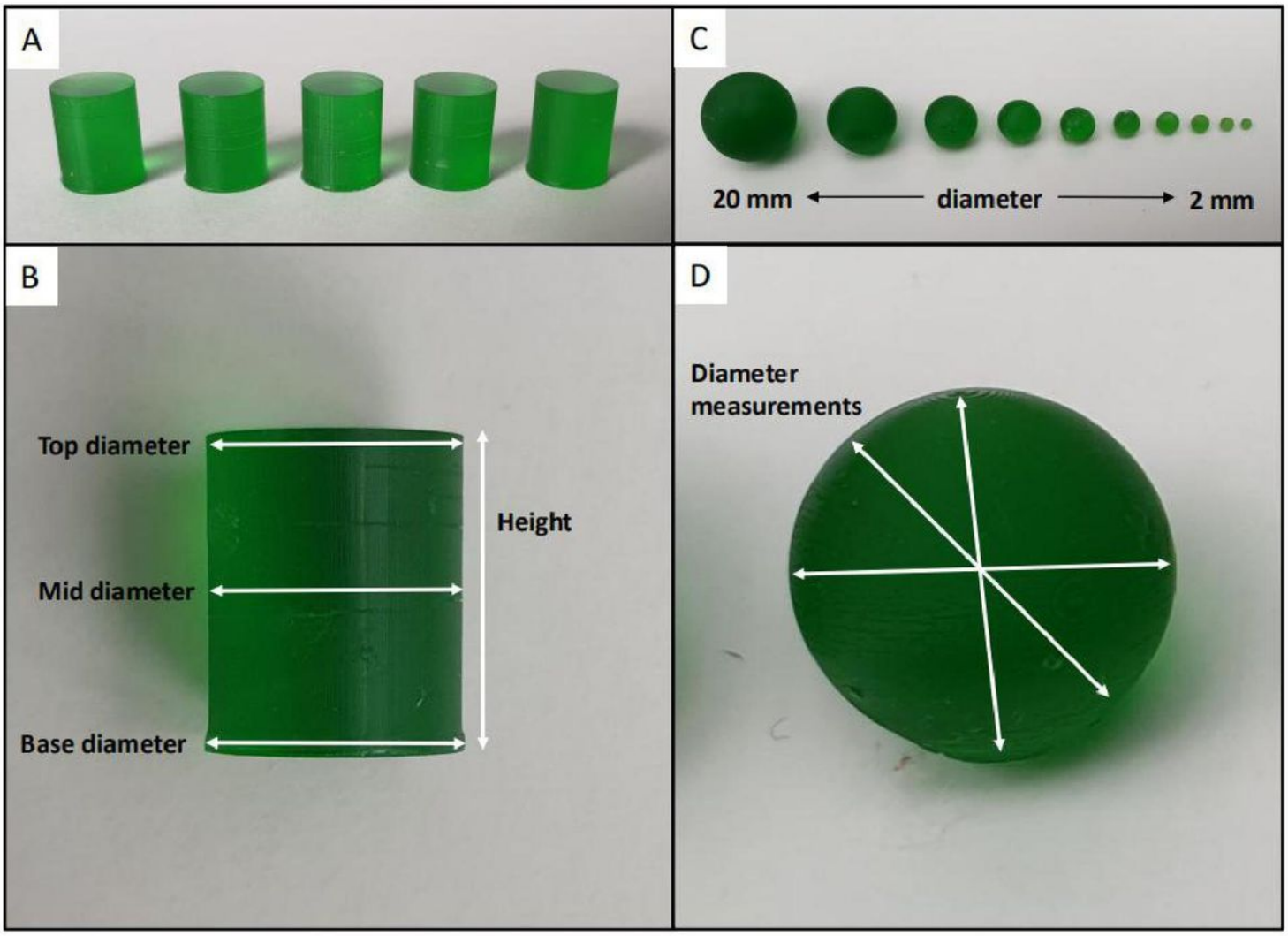

Figure 2

Example of 5 out of the 20 printed cylinders [A] and the dimensions that were measured on each cylinder [B]. The printed spheres had nominal diametersof 20, 15, 12, 10, 8, 6, 5, 4, 3 and 2 mm[C] which were measured after printing at multiple orientations [D].

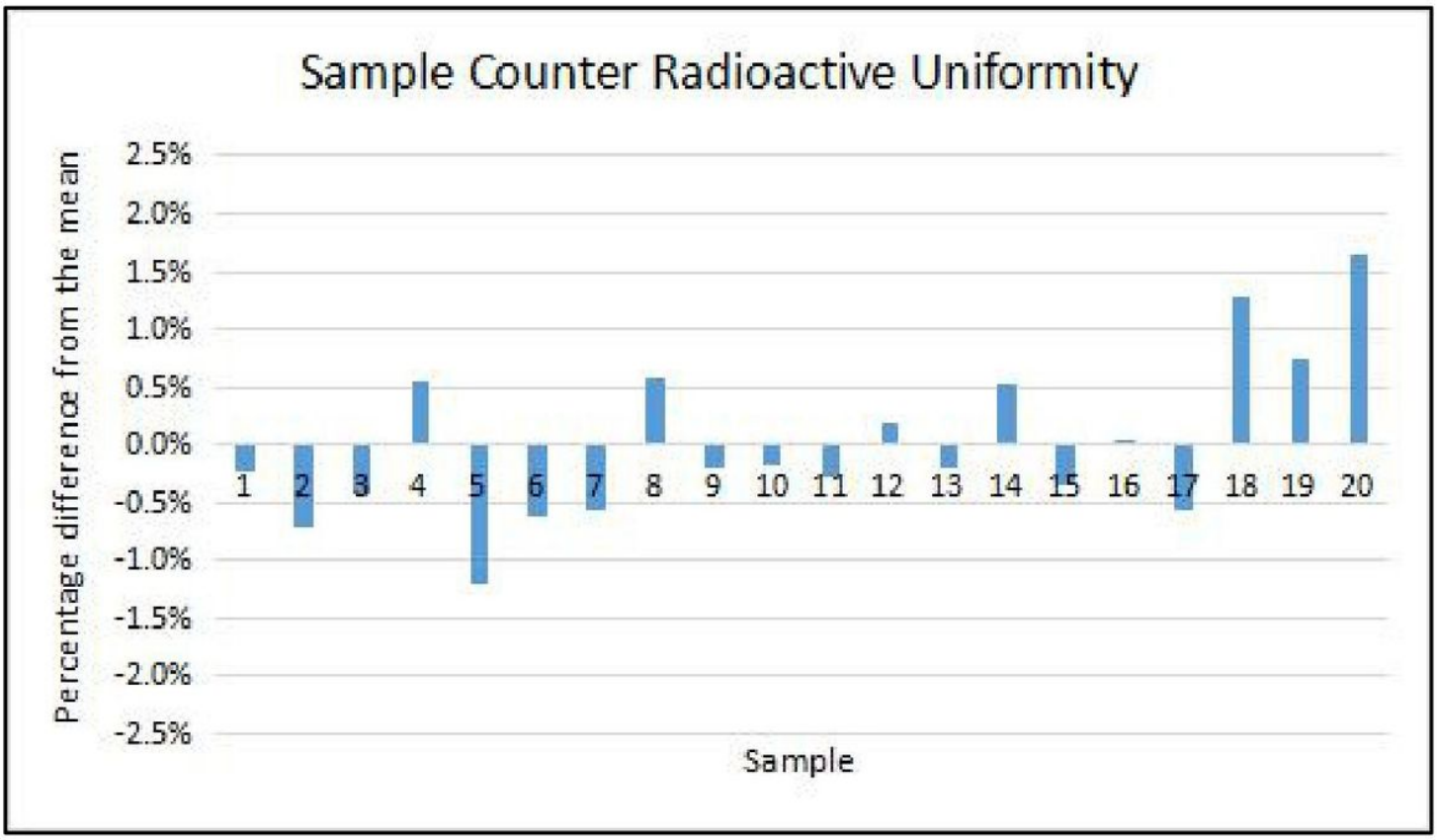

Figure 3

Chart showing the percentage differences from the mean counts acquired by the sample counter

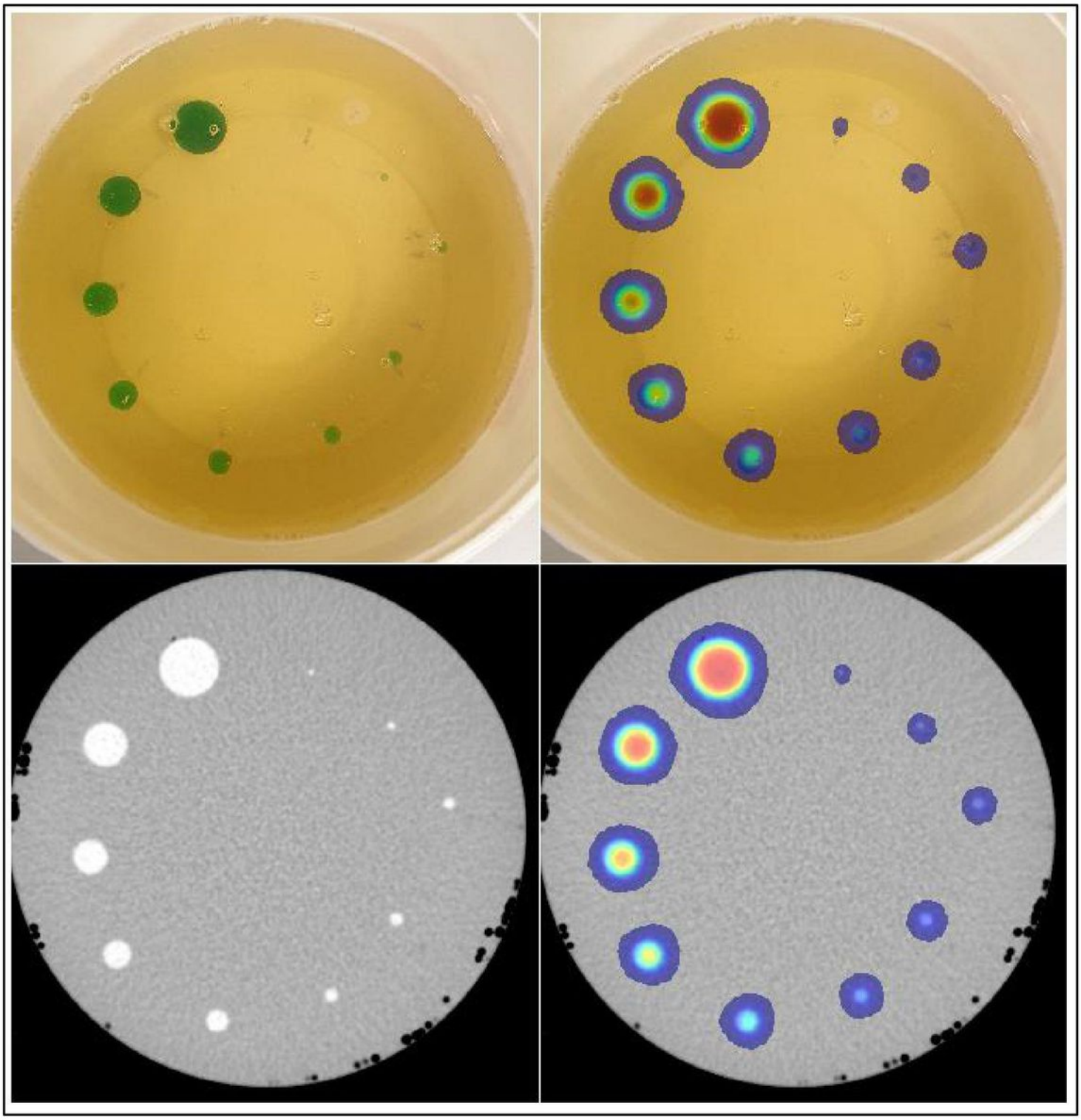

Figure 4

A - Spheres in gelatin mixture, B - Spheres in gelatin mixture with PET signal overlaid, C - CT of spheres and D - PET/CT images of spheres.

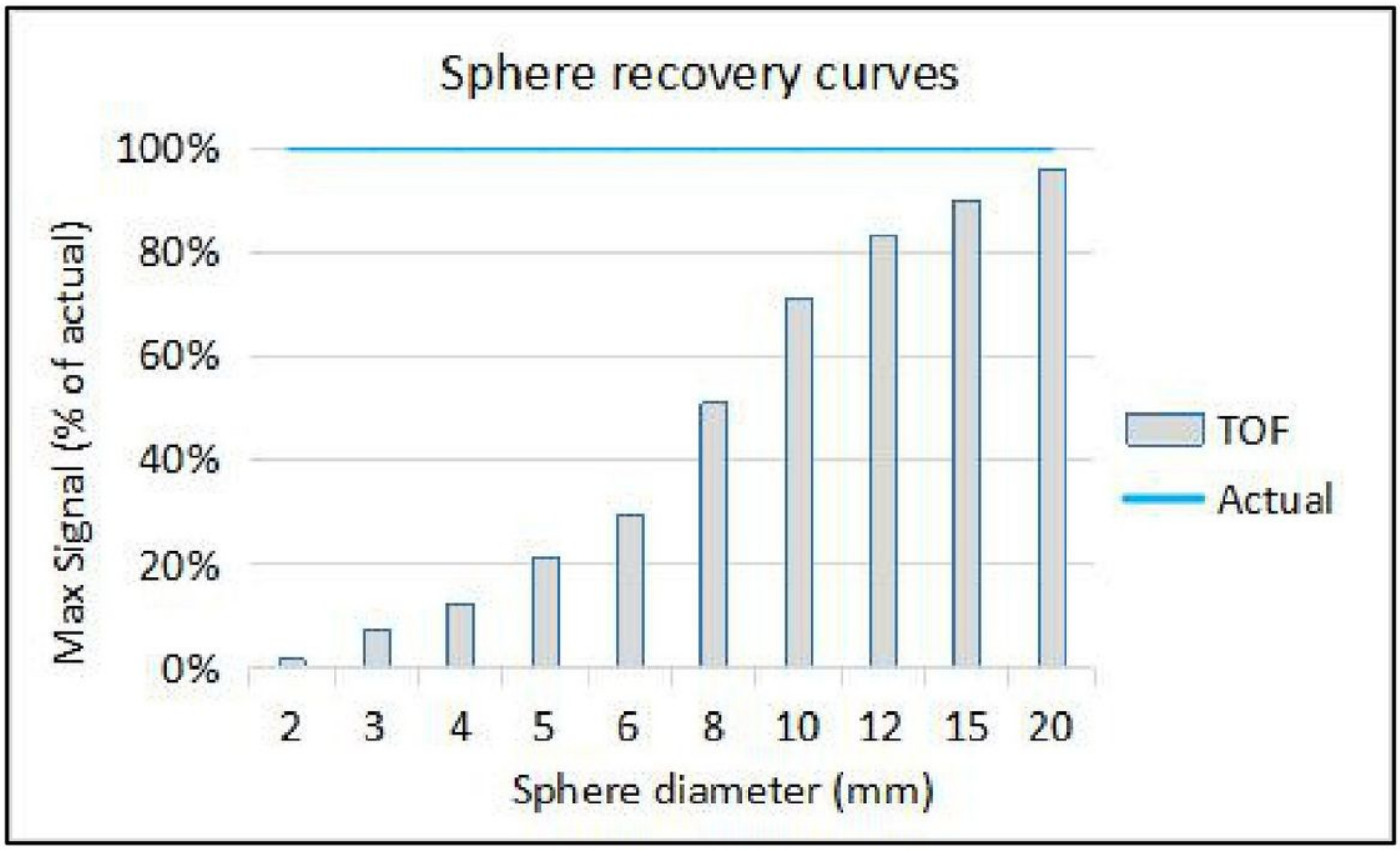

Figure 5

Bar chart showing the max signal from each sphere compared with the actual concentration

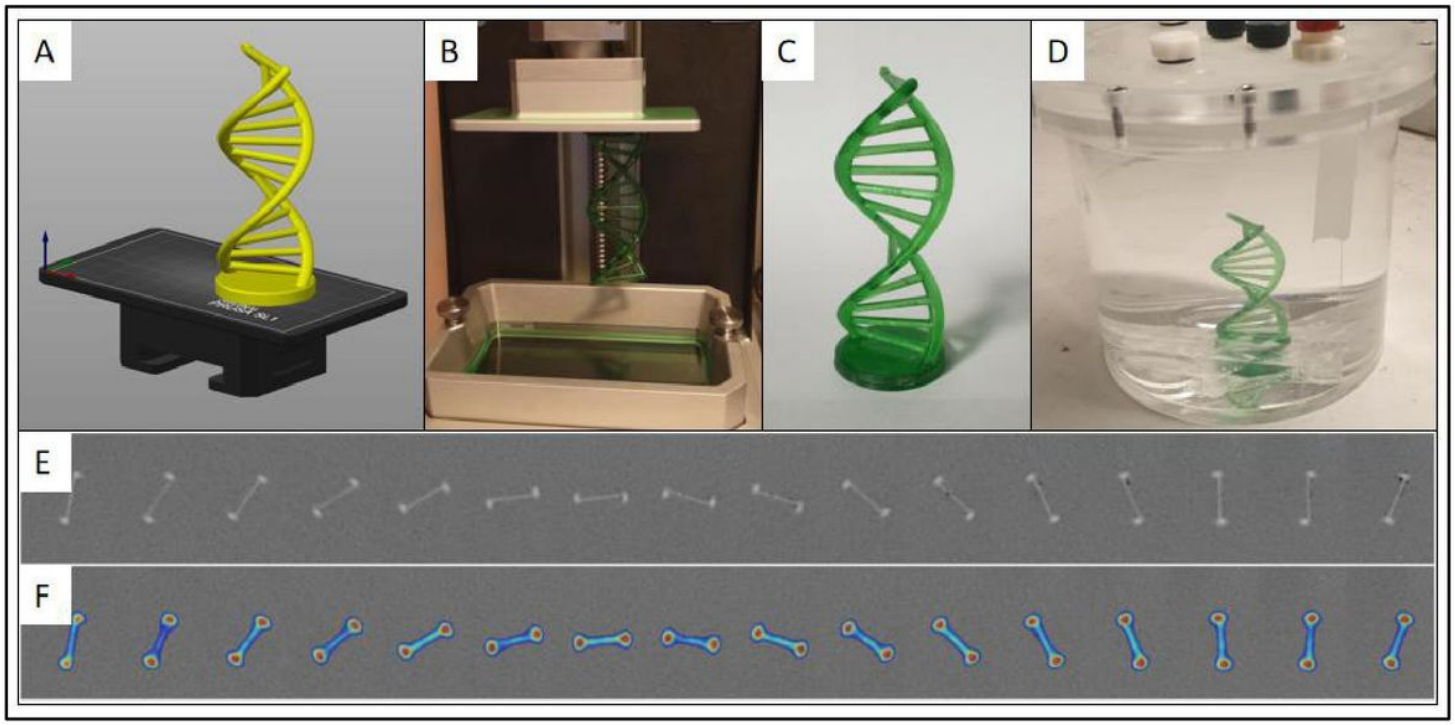

Figure 6

A - Helix model prepared for printing in PrusaSlicer. B - Helix after printing. C - Helix after removal from build plate, washed, dried and cured. D - Helix mounted in a cylinder of water for imaging. E - Axial CT slices. F - Axial PET/CT slices.

Advantages	Limitations
• No inactive walls • Accurate geometry • Can print complex 3D shapes • Short print times	• Cannot print large solid objects • Phantoms are single use • Small amount of radioactivity leaching into water • Cannot print hollow objects without an exit hole

Figure 7

Advantages and limitations of radioactive 3D printing technique